

# Directionally Cracked Mesoporous Colloidal Films by Manipulating Notch Angles and Their Anisotropic Wicking Behavior

Yunchan Lee, Min-Gi Jo, Seongwoo Jeon, Chorong Kim, Jaekyoung Kim, Sanghyuk Wooh, Kee-Youn Yoo,\* and Hyunsik Yoon\*

Wicking in porous media, such as the spreading of ink on paper or the absorption of moisture by fabric, occurs when water interacts with hydrophilic porous materials through capillary action and evaporation. The directional nature of the wicking phenomenon can be leveraged for various advanced applications, including enhanced heat transfer, colorimetric devices, energy harvesting, and microfluidics. Herein, crack generation is used to induce the anisotropic wicking of water on isolated mesoporous strips. The strips are fabricated by transforming isotropic cracks into anisotropic ones in micropyramid arrays using the *Poisson* effect in elastomeric blocks. Stretching an elastomeric block increases the period of a pyramid array along one direction while decreasing it in the perpendicular direction because of elastomer shrinkage. This amplifies the difference in the notch angles of pyramidal edges between parallel and perpendicular directions relative to the stretching axis. Consequently, the disparity in notch angles leads to preferential crack generation owing to elevated stress localization on the sharpened notches. Directional wicking is demonstrated using anisotropic strips of mesoporous TiO<sub>2</sub> colloidal films and highly anisotropic wicking of ink is illustrated by coating hydrophobic films on mesoporous strips. The anisotropic wicking observed in cracked mesoporous strips can serve as 1D microfluidic channels.

energy harvesting,<sup>[5,6]</sup> microfluidics,<sup>[7]</sup> and colorimetry<sup>[8]</sup> in medical usage. Recently, directional wicking has been investigated for effective liquid transport on surfaces and in porous media.<sup>[9–11]</sup> Directional transportation of liquids can be utilized for applications such as water harvesting, precise printing, and biosensors.<sup>[12]</sup> Furthermore, nature-inspired anisotropic features have been harnessed for anisotropic or directional liquid transport.<sup>[13–17]</sup>


Conventional microfabrication methods based on photolithography<sup>[18]</sup> are commonly employed to achieve anisotropic features. However, these methods require sophisticated equipment such as dry etchers to transfer patterns onto the underlying films. Additionally, photolithography is unsuitable for creating patterns of porous films because of the potential penetration of the photoresist into the pores. Other methods used for preparing anisotropic structures include the buckling of surfaces and crack generation by applying compressive stress and tensile strain, respectively.<sup>[19]</sup>

Oxygen plasma or ultraviolet–ozone treatment can form thin silicate layers on polydimethylsiloxane (PDMS) after stretching the PDMS films in the lateral direction. When the pre-strain is released, compressive stress can be applied to the surfaces, which buckles in the direction perpendicular to stretching. The challenge for buckles in directional wicking or imbibition is the difficulty in controlling the liquid flow owing to their low aspect ratio. Applying a tensile strain to generate cracks can

## 1. Introduction

Water wicking in porous media is a phenomenon that is often observed in daily life. Writing with ink on paper and sweat absorption by fabrics via capillary wicking for rapid drying are some examples. For decades, researchers have investigated the capillary wicking of porous materials.<sup>[1–3]</sup> In engineering applications, liquid wicking can be used for heat transfer,<sup>[4]</sup>

Y. Lee, H. Yoon  
Institute of Energy and Environment System  
Seoul National University of Science and Technology  
Seoul 01811, Republic of Korea  
E-mail: hsyoon@seoultech.ac.kr

 The ORCID identification number(s) for the author(s) of this article can be found under <https://doi.org/10.1002/ssstr.202400159>.

© 2024 The Author(s). Small Structures published by Wiley-VCH GmbH. This is an open access article under the terms of the Creative Commons Attribution License, which permits use, distribution and reproduction in any medium, provided the original work is properly cited.

DOI: 10.1002/ssstr.202400159

M.-G. Jo, S. Jeon, C. Kim, K.-Y. Yoo, H. Yoon  
Department of Chemical and Biomolecular Engineering  
Seoul National University of Science and Technology  
Seoul 01811, Republic of Korea  
E-mail: kyoo@seoultech.ac.kr

J. Kim, H. Yoon  
Department of Energy and Chemical Engineering  
Seoul National University of Science and Technology  
Seoul 01811, Republic of Korea

S. Wooh  
School of Chemical Engineering and Materials Science  
Chung-Ang University  
84 Heukseok-ro, Dongjak-gu, Seoul 06974, Republic of Korea

form anisotropic trenches, which can exhibit anisotropic liquid transport on the surfaces. However, the location of crack formation has not been controlled.

Previous studies have reported that soft lithography can be used to prepare textured colloidal films for the precise control of crack generation.<sup>[20,21]</sup> Cracks were generated on the fabricated V-shaped TiO<sub>2</sub> colloidal films during calcination because of the tensile stress originating from the volume shrinkage when the organic moiety was removed from the colloidal films. The V-shaped notches acted as initiation tips for crack generation by concentrating the tensile stress on that position.<sup>[20,21]</sup> However, as cracks were generated on all notches, advanced approaches were deemed necessary to control the position or direction of crack generation.

In this study, we consider the generation of preferential cracks from the disparity observed in notch angles across different orientations. The variations in notch angles across different orientations were generated by laterally stretching elastomeric blocks featuring micropyramids on their surfaces. Consequently, the notch angles located at the pyramidal edges increased in the stretched direction because of the tensile strain. Conversely, the notch angles decreased in the direction perpendicular to stretching owing to the shrinkage caused by the *Poisson* effect of elastomers. After replicating the stretched micropyramids on the surface of the elastomeric block, soft molding was implemented to imprint the anisotropic pyramid arrays onto the TiO<sub>2</sub> paste coated on a substrate. We performed calcination to remove all organic compounds and induced the formation of preferential cracks only at the sharper notches rather than at the blunt ones. Selectively controlled cracks were used to connect the mesoporous strips in the stretching direction while remaining isolated in the direction perpendicular to stretching. These selectively cracked mesoporous films were used to demonstrate the anisotropic wicking of liquids on the surface. The cracked mesoporous strips exhibited anisotropic hemiwicking behavior along the

cracks, and the strips were transferred onto a flexible substrate. The bent film surface exhibited anisotropic wicking after contact with a colored ink. Furthermore, highly anisotropic wicking behavior was observed on the mesoporous strips by coating hydrophobic layers on their surfaces. These mesoporous films with anisotropic cracks can be used for potential applications in various fields, including microfluidics, bioassays, and displays.

## 2. Results and Discussion

### 2.1. Selective Cracking to Fabricate Deep Microtrenches

Figure 1a illustrates the changes observed in the notch angles of the pyramid-patterned elastic PDMS blocks when a tensile strain is applied via lateral stretching. Before elastic deformation, the notch angle of the pyramid pattern is defined as  $\theta$ , which lies between the pyramids. In this study, we employed a pyramid pattern with a  $\theta$  value and width of 90° and 30  $\mu$ m, respectively (Figure S1, Supporting Information). The stretching direction was defined as the  $x$  direction with notch angle  $\alpha$ , and the perpendicular direction was designated as the  $y$  direction with notch angle  $\beta$ . Owing to the limited change in volume during deformation, the increase in the  $x$  axis resulted in the decrease in the  $y$  axis because of the shrinkage in the  $y$  direction; this is referred to as the *Poisson* effect. Consequently, the notch angle ( $\alpha$ ) in the  $x$  direction increased, whereas the angle ( $\beta$ ) in the  $y$  direction decreased. To obtain the stretched pyramid shapes with other materials, such as polyurethane acrylate (PUA), we replicated the PDMS shapes twice using soft lithography with photocurable polymers as shown in Figure S2, Supporting Information. The variations in pyramid angles were utilized by introducing the concept of preferential crack generation to fabricate deep microtrenches. The schematics in Figure 1b and S2, Supporting Information, outline the experimental procedure used for creating pyramidal structures with TiO<sub>2</sub> colloidal films

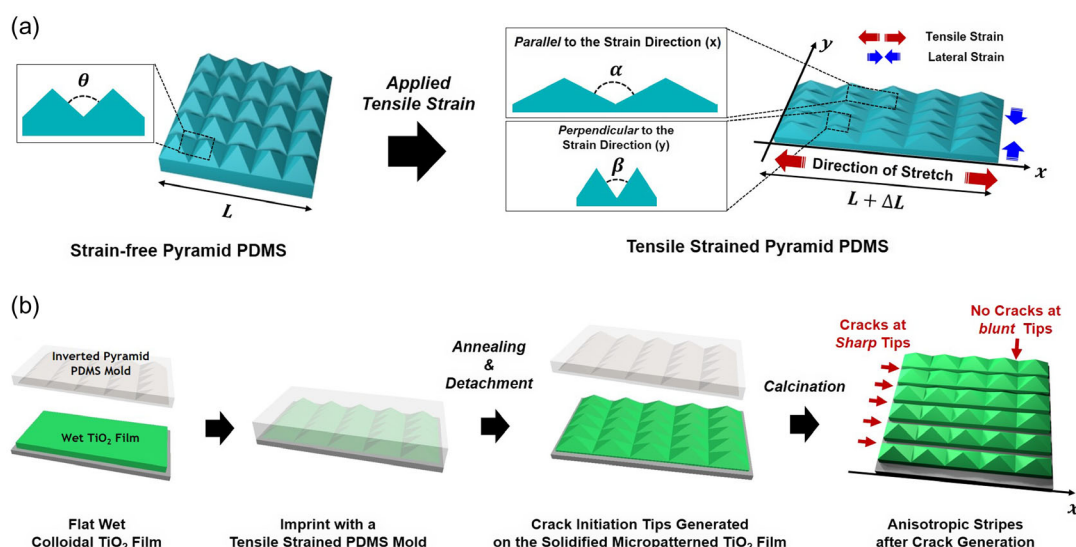


**Figure 1.** a) Schematic of asymmetric deformation of the square pyramid-patterned polydimethylsiloxane (PDMS) block after the application of tensile strain. The angles between two pyramids change anisotropically depending on the direction. b) Schematic of imprinting asymmetric pyramid pattern on the wet TiO<sub>2</sub> colloidal film and the formation of anisotropic strips after crack generation.

and for generating selective cracks across different orientations. Initially, a flat colloidal film was prepared on the substrate by applying a commercial  $\text{TiO}_2$  nanoparticle paste using the doctor blading technique; the paste was composed of  $\approx 20$  nm  $\text{TiO}_2$  nanoparticles and organic compounds. Additionally, we prepared an inverted micropillar PDMS mold with varying notch angles, replicated from the as-prepared PUA. The PDMS mold was positioned on the wet  $\text{TiO}_2$  film and maintained for 30 min to fill the voids in the mold via capillary force.<sup>[22]</sup> Subsequently, the samples were annealed at 60 °C for 30 min to remove the solvent. The annealing process resulted in the formation of either blunt or sharp initiation tips at the edges of the pyramids. The cracks did not form during the annealing process because of the constraint enforced on the  $\text{TiO}_2$  films by the PDMS mold. Subsequently, the PDMS mold was detached from the  $\text{TiO}_2$  patterns, which were then subjected to calcination at 500 °C to eliminate all organic compounds. No cracks were observed along the  $x$  axis after calcination, whereas cracks were generated along the  $y$  axis. This preferential crack generation facilitated the fabrication of anisotropic mesoporous strips isolated by cracks.

## 2.2. Manipulating Notch Angles in Micropillars on Surfaces of Elastomers

We investigated the variations in the notch angle with respect to the applied strain and compared the replicated PUA samples

obtained from the stretched PDMS. The top view of the scanning electron microscopy (SEM) images (Figure 2a–d) indicates that the square pyramids transformed into rectangular pyramids as the applied tensile strain increased from 0% to 75%. The dashed red squares in Figure 2 represent the original square pyramids, and the anisotropic parameter is defined as the length-to-width ratio of the unit pyramids. The pristine PDMS blocks featured square pyramid patterns with dimensions of  $30 \times 30$   $\mu\text{m}$ , resulting in an anisotropic parameter of 1 (Figure 2a). At tensile strains of 25%, 50%, 75%, and 100%, the anisotropic parameters increased to 1.16, 1.57, 2, and 2.33, respectively (Figure 2b–d and S3a, Supporting Information). The angular differences between the two pyramids were examined at each tensile strain. The pristine pyramidal PDMS block exhibited notch angles of 90° in both directions (Figure 2e). However, the notch angles diverged into two distinct values in each direction when a tensile strain was applied to the PDMS blocks. In the  $x$  direction, the angles increased to 99°, 114°, 134°, and 147° as the applied tensile strain increased to 25%, 50%, 75%, and 100%, respectively (Figure 2f–h and S3b, Supporting Information). In the  $y$  direction, the angles decreased to 87°, 87°, 82°, and 75° as the applied tensile strain increased to the same levels (Figure 2i–k and S3c, Supporting Information). Figure 2l illustrates the finite-element method (FEM) simulation results when 100% strain is applied, wherein the initial angle is increased and decreased to 150° and 75° in the  $x$  and  $y$  directions, respectively. The numerical parameters considered during the simulation included Young's

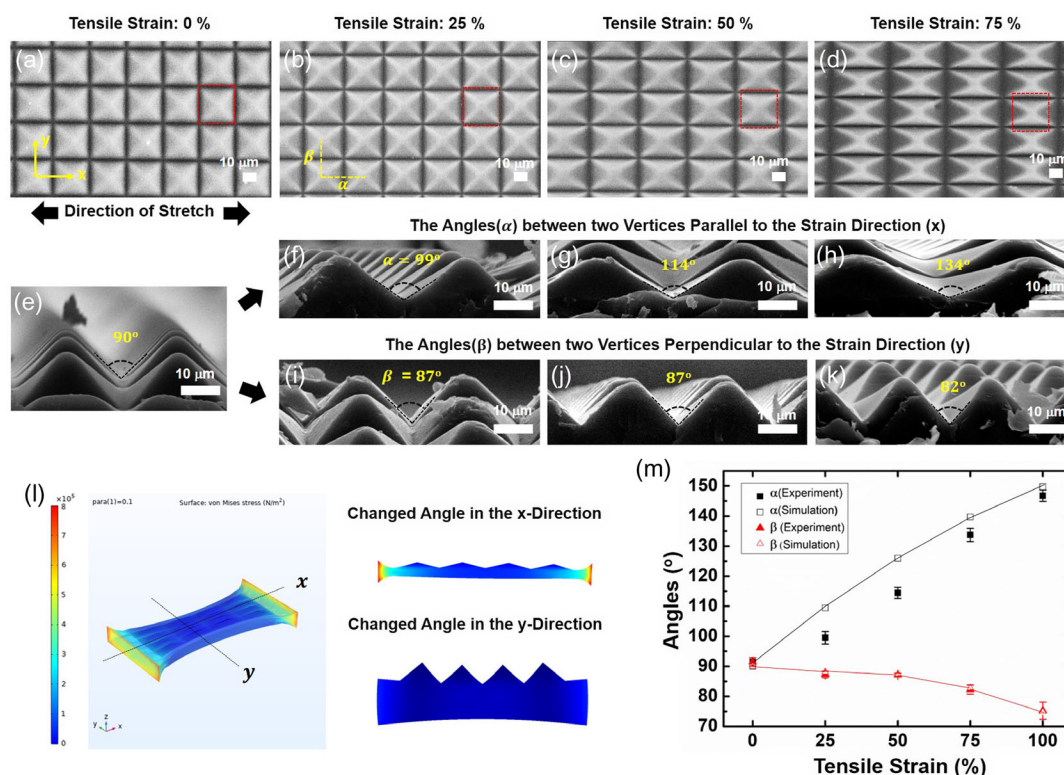


**Figure 2.** Top view of the scanning electron microscopy (SEM) images of the polyurethane acrylate (PUA) replicated from strained polydimethylsiloxane (PDMS): a) 0%, b) 25%, c) 50%, and d) 75%. e) The initial notch angle without strain increased in the  $x$  direction: f) 25%, g) 50%, and h) 75%, whereas it decreased in the  $y$  direction: i) 25%, j) 50%, and k) 75%. l) The finite-element method (FEM) simulation results after applying 100% strain to the square pyramid-patterned PDMS block. m) Plot of angle variations as a function of the tensile strain.

modulus of PDMS, Poisson's ratio, and width and inclination parameters of the pyramid pattern. The plot in Figure 2m illustrates the results for the other strains and reveals strong agreement between the experimental and simulation results.

### 2.3. Effect of Notch Angle and Film Thickness on Crack Generation

Figure 3 depicts  $\text{TiO}_2$  films featuring elongated pyramid patterns, replicated using the inverse pyramidal PDMS mold (Figure 2). When the  $\text{TiO}_2$  paste was imprinted with an inverted pyramidal PDMS mold replicated at 100% strain, a blunt initiation tip was formed in the  $x$  direction at an angle of  $153^\circ$  (Figure 3a), whereas a sharp tip was formed in the  $y$  direction at an angle of  $97^\circ$  (Figure 3b). In a previous study, we observed that cracks were generated during calcination, a process used for removing all organic compounds; this resulted in a weight loss of  $\approx 40\%$  and a volume shrinkage of  $\approx 20\%$  in the film.<sup>[21]</sup> In this study, our objective was to induce selective crack formation by leveraging the differences in stress localization at notches with varying angles. After performing calcination at  $500^\circ\text{C}$ , no cracks were observed in the blunt notches (Figure 3c); however, cracks were generated in the sharp notches (Figure 3d). Figure 3e–g displays the top view of the SEM images of calcinated  $\text{TiO}_2$  films

with residual thicknesses of  $\approx 4.5\ \mu\text{m}$ , prepared by replicating deformed patterns from stretched PDMS blocks at 0% (Figure 3e), 50% (Figure 3f), and 100% (Figure 3g) tensile strains. Here, the residual layer was the minimum thickness of a  $\text{TiO}_2$  film remaining after soft molding. As the strain increased, the square pyramidal structures transformed into rectangles. Simultaneously, cracks propagated in every notch in both the  $x$  and  $y$  directions until the strain reached 50%, resulting in the isolation of the square and rectangular pyramids. Furthermore, cracks were exclusively generated parallel to the  $x$  direction at a tensile strain of 100%, leading to the formation of isolated structures with microtrenches (Figure 3g).

Figure 3h–j indicates the cross-sectional SEM images of the  $\text{TiO}_2$  films after calcination. Isotropic cracks were generated in both the  $x$  and  $y$  directions within the films imprinted using the PDMS mold until a tensile strain of 50% was applied (Figure 3h). When imprinted with a 75% strained PDMS mold, stresses began to localize only on relatively sharp notches, and both non-cracked and cracked notches (referred to as mixed cracks) were generated among the blunt notches (Figure 3i and S4, Supporting Information). Eventually, no cracks were generated on any of the blunt notches when imprinted with a PDMS mold strained to 100%, whereas cracks were generated on all sharp notches, which induced unidirectional cracks within the films

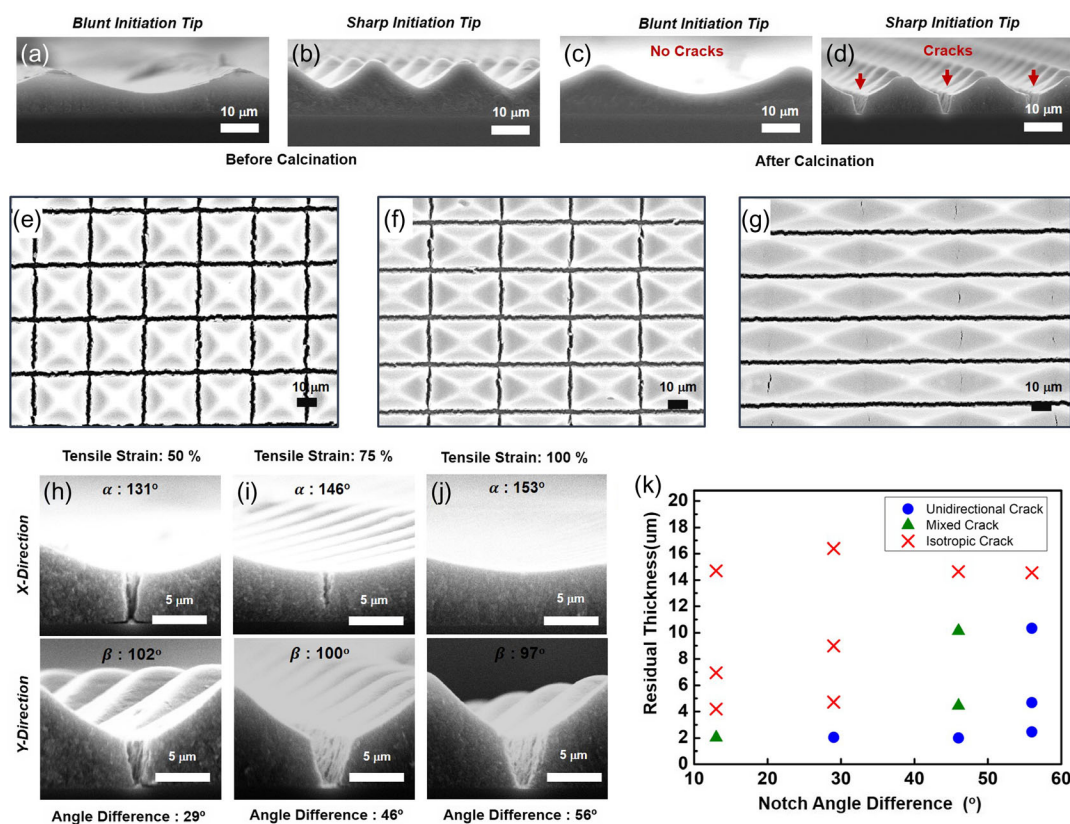


**Figure 3.** Scanning electron microscopy (SEM) images of the blunt initiation tip formed a) before and c) after calcination. The SEM images of the sharp initiation tip formed b) before and d) after calcination. The cracks observed only at the sharp initiation tip. The top view of the SEM images inducing anisotropic cracks controlled by notch angles under different strains: e) 0%, f) 50%, and g) 100%. The cross-sectional SEM images of induced unidirectional cracks under different strains: h) 25%, i) 50%, and j) 100%. k) Diagram of the relationship between the notch angle difference and residual layer thickness during crack generation.



(Figure 3j). We note that cracks initiating at the notch could propagate to the substrate, as shown in Figure S5, Supporting Information. We further investigated the residual thickness required to induce unidirectional cracks at various angle differences because film thickness is a factor that determines the stress in drying colloidal films.<sup>[21,23]</sup> Figure 3k illustrates the relationship between the angle difference and crack generation, which indicates that a larger angle difference intensifies the stress localized at the sharp edges, thereby increasing the residual layer film thickness and inducing unidirectional cracks. For instance, anisotropic crack formation was observed at a residual thickness of 4.7  $\mu\text{m}$ , whereas cracks propagated across channels when the film thickness was increased to 14.5  $\mu\text{m}$  (Figure S6, Supporting Information). These results offer a simple method for controlling the capacity of microchannels through thickness control.

#### 2.4. Anisotropic Wicking in Cracked Mesoporous $\text{TiO}_2$ Microchannels

The anisotropic characteristics of  $\text{TiO}_2$  films with anisotropic cracks can be harnessed for the directional wetting or wicking

of water on their surfaces. To investigate the wicking behavior of the cracked  $\text{TiO}_2$  films, we deposited 1  $\mu\text{L}$  water droplets onto the surface using a pipette and tracked the wicking distance from the center in both the  $x$  and  $y$  directions. **Figure 4a** illustrates the spreading of water on the calcinated  $\text{TiO}_2$  films patterned with pristine micropylramids. The inset depicts an optical microscopic image of the sample, revealing symmetrically generated cracks. A water droplet exhibited isotropic spreading on symmetrically cracked  $\text{TiO}_2$  films (Figure 4b). When a PDMS pattern strained by 50% in the  $x$  direction was used, anisotropic wicking behavior was observed (Figure 4c). The cracked lines became rectangular (inset image in Figure 4c), resulting in a higher wicking speed in the  $x$  direction than that observed in the  $y$  direction (Figure 4d). After forming anisotropic cracks with a 100% strained PDMS mold (Figure 4e), the wicking speed through the microtrench in the  $x$  direction significantly surpassed that in the  $y$  direction because the trenched channel offered lower resistance to water flow than the porous  $\text{TiO}_2$  films (Figure 4f). However, the permeation of water could not be prevented in the  $y$  direction because both the  $\text{TiO}_2$  film and substrate were hydrophilic. Figure 4g illustrates stills from the video demonstration of anisotropic wicking after a water droplet was dropped. As water

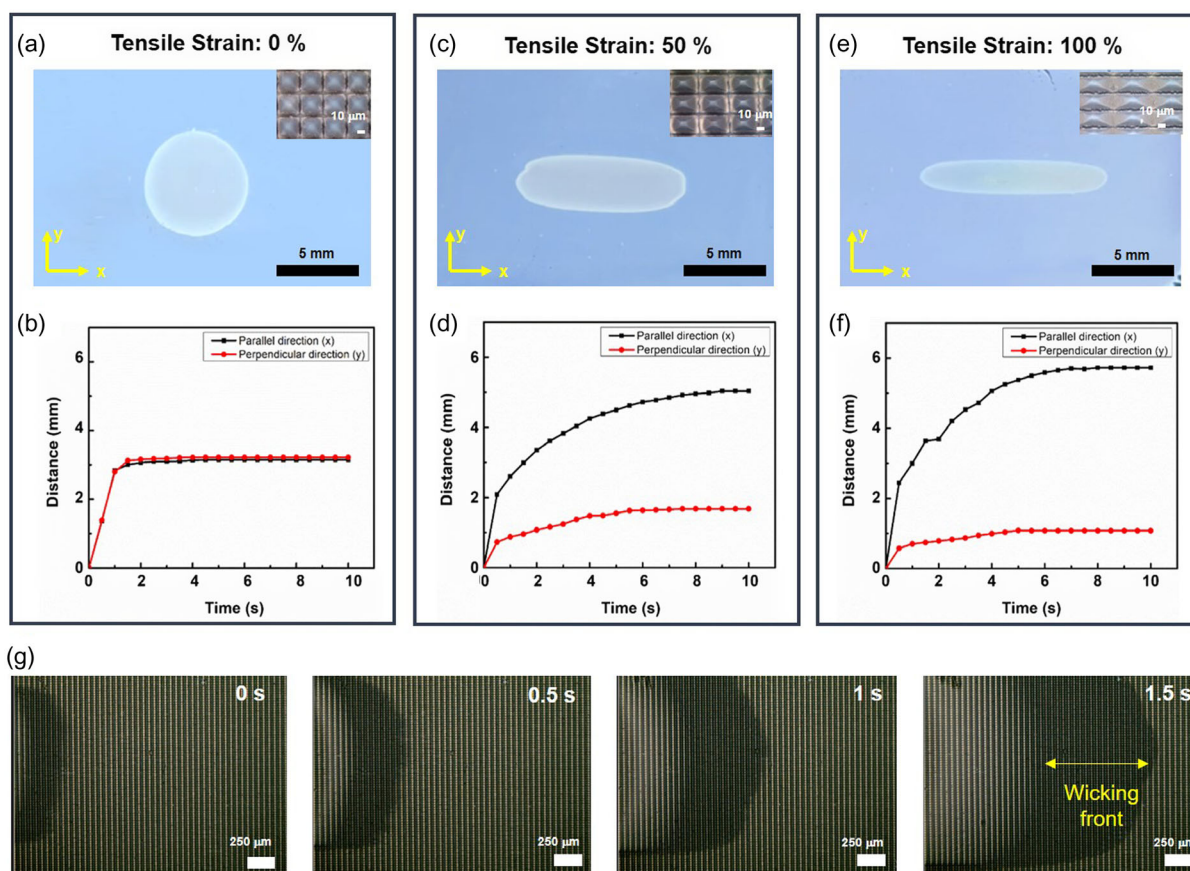


**Figure 4.** a) Image depicting water wicking on a symmetrically cracked mesoporous film. b) Graph illustrating wicking distance versus time in the  $x$  and  $y$  directions based on the wicking indicated in (a). c) Image depicting water wicking on an anisotropically cracked mesoporous film with a 50% strained polydimethylsiloxane (PDMS) pattern. d) Graph presenting wicking distance versus time in the  $x$  and  $y$  directions based on the wicking indicated in (c). e) Image displaying water wicking on a unidirectionally cracked mesoporous film. f) Graph indicating wicking distance versus time in the  $x$  and  $y$  directions based on the wicking indicated in (f). Insets in (a), (c), and (e) depict the optical microscopic images of the surface of the samples. g) Stills from the video demonstrating the anisotropic wicking of a water droplet on a unidirectionally cracked mesoporous film.

spread in the  $x$  direction, the wicking front filled with water, becomes wider. The microtrenches between the mesoporous strips facilitated rapid water transport, while water permeated into the porous strips in the  $y$  direction, perpendicular to the cracks. Figure S7 and S8, Supporting Information, demonstrate the repeatability and long-term stability of the anisotropic wicking behavior.

We then transferred the mesoporous strips to a flexible substrate to present their potential application. After the preparation of the unidirectionally cracked mesoporous strips on a glass substrate, the cracked films were attached to an adhesive tape bonded on a polyethylene terephthalate (PET) film (Figure 5a). Then, they were detached from the glass substrate and the mesoporous films were transferred onto the PET film. Figure 5b depicts an image of a cracked mesoporous film prepared on a glass substrate, and Figure 5c shows the image of the transferred film on the PET film. The SEM images (Figure 5d,e) confirmed that the mesoporous strips were isolated well. Blue ink was dropped onto a bent PET film after preparing the mesoporous strips; the ink wicked in the parallel direction of the cracks (Figure 5f). To demonstrate the directional liquid flow of small droplets, flexible mesoporous strips were brought in contact with a droplet of red ink (Figure 5g). Anisotropy was observed even after the ink was transferred to the flexible film. The strips were bent perpendicular to the cracks to prevent the formation of additional cracks during bending. The ability to direct the flow of small biofluid droplets, such as blood, shows promise for applications in diagnostic bioassays.

We applied a coating of hydrophobic polymers on the surface to achieve a highly anisotropic wicking suitable for microfluidic channels. Deep microtrenches coated with hydrophobic materials served as barriers to prevent water from flowing across the trench. As depicted in Figure 6a, polystyrene (PS) was spin-coated on the cracked  $\text{TiO}_2$  films. Figure 6b depicts the contact angles of the substrate and mesoporous  $\text{TiO}_2$  films before and after spin-coating a high molecular weight (Mw of  $\approx 192\,000$ ) 5 wt% PS solution dissolved in toluene. Before spin-coating, both the substrate and  $\text{TiO}_2$  films exhibited contact angles of less than  $30^\circ$ , indicating hydrophilicity. However, the contact angle on the substrate was  $\approx 90^\circ$  after spin-coating the PS layers, indicating hydrophobicity. The contact angle on mesoporous  $\text{TiO}_2$  remained at  $\approx 30^\circ$ , maintaining hydrophilicity due to the presence of porosity. As shown in the high-resolution SEM image in Figure S9a, Supporting Information, the porosity of the  $\text{TiO}_2$  strips is preserved after coating with a 5 wt% PS solution. However, the pore size is not small enough to prevent PS from penetrating the mesoporous strips. Figure S9b, Supporting Information, demonstrates that more PS chains are present in the porous strips when the concentration of the PS solution is increased to 20 wt%.

After the preparation of PS-coated samples, water wicking was demonstrated on isolated mesoporous pyramids (Figure 6c) and isolated mesoporous strips (Figure 6d). Blue-dyed water, stained with trypan blue, was injected using a 1 mL syringe equipped with a glass capillary needle with an internal diameter of  $20\,\mu\text{m}$  (Figure 6e). The hydrophobic PS-coating prevented the blue ink water from wicking through the isolated microstructure,

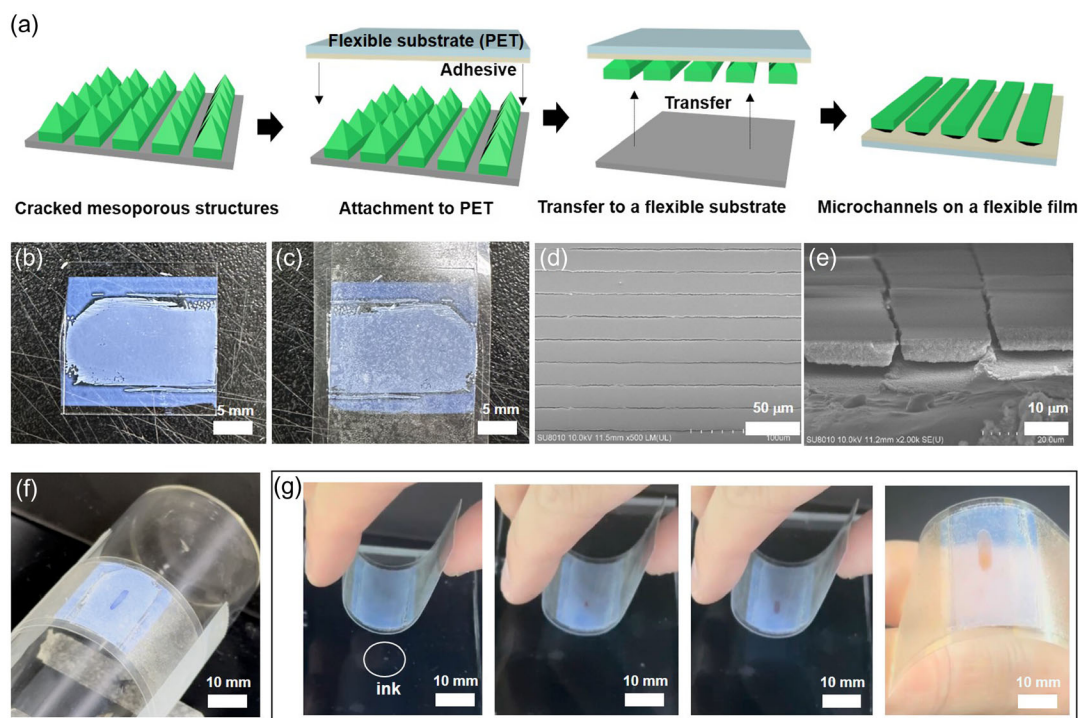


**Figure 5.** a) Schematic of the experimental procedure of transferring mesoporous strips onto a flexible substrate. b) Image of a  $\text{TiO}_2$  mesoporous film on a glass substrate after anisotropic crack generation. c) Image of the mesoporous film transferred onto a polyethylene terephthalate (PET) film. d) Scanning electron microscopy (SEM) image of mesoporous strips on the flexible film depicted in (c). e) Cross-sectional SEM image of mesoporous strips transferred onto a flexible film. f) Anisotropic wicking of blue ink. g) Stills from the video demonstrating the anisotropic wicking on a flexible film after contact with an ink droplet.

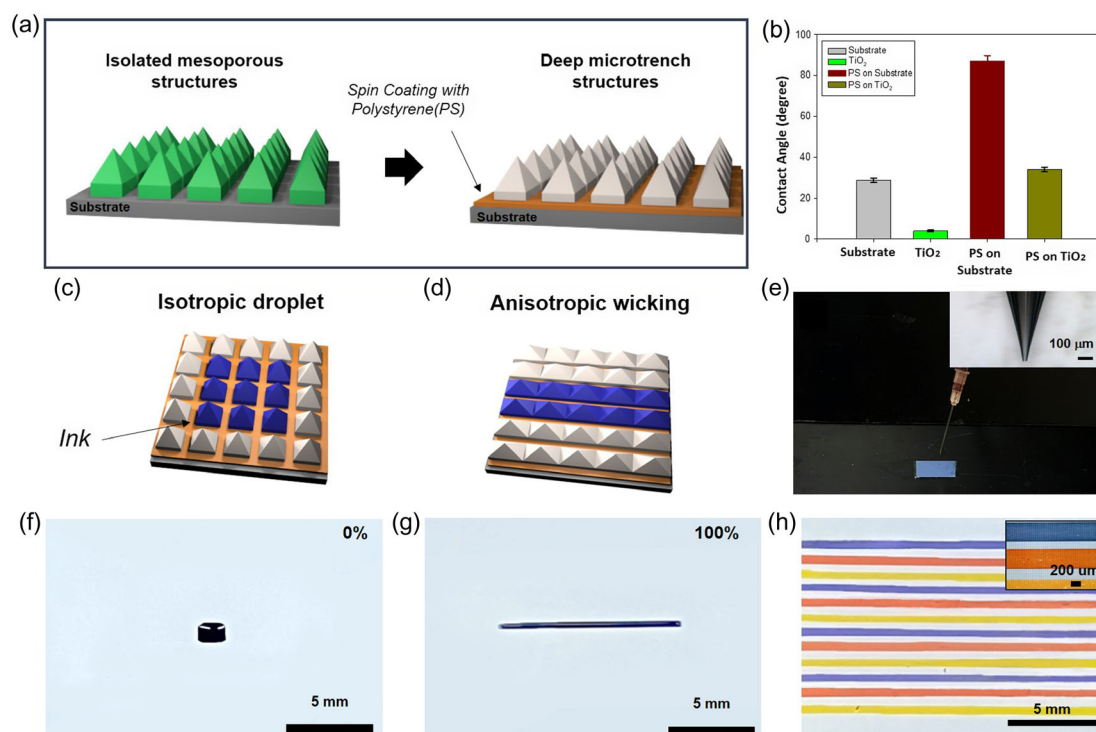


**Figure 6.** a) Schematic of the coating of a hydrophobic polystyrene (PS) layer that isolates mesoporous patterns. b) Contact angles of the substrate surface and mesoporous TiO<sub>2</sub> before and after coating with PS. c) Schematic of isolated wicking of ink on isotropically cracked mesoporous pyramids isolated by a PS layer. d) Schematic of anisotropic wicking of ink on anisotropically cracked mesoporous strips isolated by a PS layer. e) Picture shows the method of injecting water ink on film and optical microscopy image of the glass capillary needle attached to the front of the needle. Demonstration of anisotropic wicking of ink with different strains: f) 0% and g) 100%. h) Optical images demonstrating a microchannel with three repeated different colored strips.

resulting in a symmetric behavior at 0% strain (Figure 6f). However, at 100% strain, the blue ink water was wicked parallel to the  $x$  direction through the connected mesoporous TiO<sub>2</sub> microstructure (Figure 6g). The entire surface transitioned to hydrophobicity when the mesoporous strips were coated with a 20% PS solution (2.14 μm thick), as illustrated in Figure S10, Supporting Information. Additionally, directional wicking was observed after the application of other hydrophobic films, such as polymethylmethacrylate (Figure S11, Supporting Information). Furthermore, we demonstrated a microchannel with three repeated strips of different colors, namely, red, orange, and blue (Figure 6h). This indicates that microstructures that are isolated unidirectionally by cracks are essential prerequisites for obtaining microchannels.

### 3. Conclusions

In this study, we fabricated TiO<sub>2</sub> films with unidirectional cracks by manipulating notch angles in different orientations. A tensile strain was applied to a square pyramidal PDMS block to control both the anisotropic shape and notch angles. The stretched pyramid patterns were transferred to a TiO<sub>2</sub> wet colloidal film using the soft imprinting method, and anisotropic pyramidal TiO<sub>2</sub> structures were formed after film calcination. The notches induced cracks by concentrating the stress during calcination.

Cracks were generated at sharp notch angles, whereas no cracks were observed at blunt notch angles, which were replicated by stretching PDMS at a high strain rate. We demonstrated unidirectional wicking using anisotropic mesoporous structures. At high strains, cracks were generated in only one direction and the mesoporous microstructures were connected in the parallel direction, whereas they were separated in the perpendicular direction. Therefore, we manipulated the 1D micro-strips to show anisotropic wicking in a rigid or flexible substrate. We believe that the proposed method of fabricating mesoporous microchannels composed of TiO<sub>2</sub> pyramidal microstructures can be easily applied in various fields, such as microfluidics, colorimetry, and photocatalytic reactions.

### 4. Experimental Section

**Deformation and Replication Process of Pyramidal PDMS:** PDMS prepolymer with 15:1 wt% mixture (base:curing agent) was poured into an inverted pyramid and cured at 60 °C for 8 h. The PDMS block with dimensions of 2.5 × 2.5 cm and a square pyramid pattern was placed in a pulling machine. The applied tensile strain ranged from 0% to 100%. We poured a photocurable polymer (PUA 301; MCNet Co., Ltd., South Korea) onto the stretched PDMS and covered it with a PET film. After illuminating the PDMS with UV light for 5 min, the patterns on the stretched PDMS were transferred to PUA.

**Fabrication of Crack-Initiation Notches and Cracking of TiO<sub>2</sub> Films:** A wet flat TiO<sub>2</sub> colloidal film was prepared by coating a commercial paste



(18NR-T, Dyesol) using the doctor blading technique. The film thickness was controlled using two different spacers: 35 and 62.5  $\mu\text{m}$ . A PDMS mold with an inverted pyramid pattern was stamped onto the wet film and detached after drying at 60 °C for 30 min. The films were sintered at 500 °C for 20 min at a controlled heating rate to decompose the remaining organic binders. Finally, controlled cracks were formed at the patterned edges depending on the notch angles.

**FEM Simulation:** A conventional FEM software (COMSOL Multiphysics v.6.0) was used to obtain the deformation of the structure by applying a pulling force; a solid-mechanics module and a physics-controlled mesh (basic auto-mesh) were employed for the simulation. A total of 16 pyramidal structures were obtained, with the horizontal length, vertical length, and height set to 30, 30, and 15  $\mu\text{m}$ , respectively. The horizontal length, vertical length, and height of the substrate were 150, 150, and 30  $\mu\text{m}$ , respectively. PDMS was used as the material, and a pulling force of 0.001 N was applied along the x axis using a rigid connector.

**Fabrication of Microchannels by Coating a Hydrophobic Layer Between Cracks:** To ensure the separation of each isolated mesoporous  $\text{TiO}_2$  structure, a thin blocking layer of PS was coated on the cracks along the valleys. The 10 wt% PS (Mw of  $\approx 192\,000$ ; Sigma-Aldrich) was dissolved in toluene and spin-coated on the  $\text{TiO}_2$  film at 1500 rpm for 30 s. Subsequently, the substrates were heated to 70 °C for 30 min to eliminate any residual solvent. Dyed water was prepared by mixing three different dyes in water, including Congo red, methyl orange, and trypan blue. Each dyed water sample was injected using a 1 mL syringe that was equipped with a glass capillary needle.

**Characterization:** We used SEM (EM-30, COXEM, Korea) to observe the angle differences of replicated PUA and crack formations of  $\text{TiO}_2$  films. A contact angle analyzer (Phoenix-MT (A); S.E.O. Co., Ltd., Korea) was used to measure the water contact angle, and the notch angles were measured using ImageJ.

## Supporting Information

Supporting Information is available from the Wiley Online Library or from the author.

## Acknowledgements

Y.L. and M-G.J. contributed equally to this work. This work was supported by National Research Foundation of Korea (NRF) (grant no. RS-2024-00341884) and the Technology Innovation Program (grant no. 20010371) funded by the Ministry of Trade, Industry and Energy (Korea).

## Conflict of Interest

The authors declare no conflict of interest.

## Data Availability Statement

The data that support the findings of this study are available in the supporting Information of this article.

## Keywords

colloidal films, cracks, elastomers, soft lithographies, wickings

Received: April 3, 2024

Revised: August 6, 2024

Published online:

- [1] J. Kim, M. W. Moon, K. R. Lee, L. Mahadevan, H. Y. Kim, *Phys. Rev. Lett.* **2011**, 107, 2.
- [2] D. Miao, Z. Huang, X. Wang, J. Yu, B. Ding, *Small* **2018**, 14, 1801527.
- [3] J. Ha, J. Kim, Y. Jung, G. Yun, D. N. Kim, H. Y. Kim, *Sci. Adv.* **2018**, 4, eaao7051.
- [4] R. Wen, S. Xu, Y. C. Lee, R. Yang, *Nano Energy* **2018**, 51, 373.
- [5] C. Zhi, S. Shi, S. Zhang, Y. Si, J. Yang, S. Meng, B. Fei, J. Hu, *Nano-Micro Lett.* **2023**, 15, 60.
- [6] T. H. Nguyen, A. Fraiwan, S. Choi, *Biosens. Bioelectron.* **2014**, 54, 640.
- [7] R. Tang, H. Yang, Y. Gong, Z. Liu, X. J. Li, T. Wen, Z. G. Qu, S. Zhang, Q. Mei, F. Xu, *Sci. Rep.* **2017**, 7, 1360.
- [8] P. Q. Nguyen, L. R. Soenksen, N. M. Donghia, N. M. Angenent-Mari, H. de Puig, A. Huang, R. Lee, S. Slomovic, T. Galbersanini, G. Lansberry, H. M. Sallum, E. M. Zhao, J. B. Niemi, J. J. Collins, *Nat. Biotechnol.* **2021**, 39, 1366.
- [9] L. Chen, A. Ahmed Babar, G. Huang, J. Zhao, W. Yan, H. Yu, Q. Feng, X. Wang, *J. Colloid Interface Sci.* **2023**, 645, 200.
- [10] S. Jung, W. Kim, H. Y. Kim, *J. Fluid Mech.* **2021**, 915, A58.
- [11] B. Y. Liu, R. Seemann, L. J. Chen, M. Brinkmann, *Langmuir* **2019**, 35, 16476.
- [12] M. Soltani, K. Golovin, *RSC Adv.* **2020**, 10, 40569.
- [13] L. Feng, S. Li, Y. Li, H. Li, L. Zhang, J. Zhai, Y. Song, B. Liu, L. Jiang, D. Zhu, *Adv. Mater.* **2002**, 14, 1857.
- [14] H. Wu, R. Zhang, Y. Sun, D. Lin, Z. Sun, W. Pan, P. Downs, *Soft Matter* **2008**, 4, 2429.
- [15] R. Dufour, G. Perry, M. Harnois, Y. Coffinier, V. Thomy, V. Senez, R. Boukherroub, *Colloid Polym. Sci.* **2013**, 291, 409.
- [16] E. Bormashenko, Y. Bormashenko, T. Stein, G. Whyman, E. Bormashenko, *J. Colloid Interface Sci.* **2007**, 311, 212.
- [17] Y. Zheng, X. Gao, L. Jiang, *Soft Matter* **2007**, 3, 178.
- [18] D. Wu, J. N. Wang, S. Z. Wu, Q. D. Chen, S. Zhao, H. Zhang, H. B. Sun, L. Jiang, *Adv. Funct. Mater.* **2011**, 21, 2927.
- [19] D. Kwon, S. Wooh, H. Yoon, K. Char, *Langmuir* **2018**, 34, 4732.
- [20] S. Wooh, S. Lee, Y. Lee, J. H. Ryu, W. B. Lee, H. Yoon, K. Char, *ACS Nano* **2016**, 10, 9259.
- [21] Y. Lee, J. Kim, S. Lee, S. Wooh, H. Yoon, K. Char, *Langmuir* **2022**, 38, 4935.
- [22] Y. Lee, M. Jo, J. Kim, J. H. Kim, J. J. Kim, K. Char, H. Yoon, *Adv. Mater.* **2023**, 35, 2300952.
- [23] K. B. Singh, M. S. Tirumkudulu, *Phys. Rev. Lett.* **2007**, 98, 218302.